

# Thermally Tunable Absorption-Induced Transparency by a Quasi 3D Bow-Tie Nanostructure for Nonplasmonic and Volumetric Refractive Index Sensing at Mid-IR

Dihan Hasan, Chong Pei Ho, and Chengkuo Lee\*

A nonresonant transmission process namely absorption-induced transparency (AIT) is demonstrated in a quasi 3D bow-tie nanostructure at mid-IR spectrum for the first time. The quasi 3D structure is formed by self-aligning two metasurfaces obtained by the Babinet's principle which are linked to each other through a patterned layer of PMMA. It is shown that the vibrational absorption of poly(methyl methacrylate) (PMMA) at 5.79  $\mu\text{m}$  can strongly influence the propagation characteristics of the quasi 3D structure and generate the absorption-induced transmission peak. A detailed parametric study is conducted on the process and its nonplasmonic characteristics are confirmed. Later, the usefulness of the quasi 3D nanochannels of the geometry is addressed and volumetric refractive index sensing (refractive index unit (RIU) shift of 123.33 nm) by the AIT effect is experimentally demonstrated for the first time. Lastly, the thermal responsiveness of the metal–dielectric hybrid platform is exploited and a thermal tuning up to 25 nm for a moderate range of temperature increase (100°) is obtained. It is believed that the hybrid system with 3D nanochannels assisted transparency can be a new avenue for volumetric plasmonic sensing and stimuli responsive device operating solely on the principle of changing molecular conformation of material.

harvesting, telecom, and sensing industries.<sup>[1–6]</sup> Controlled transmission of light, which has been attractive for centuries since the invention of the camera obscura, is an important subtopic of plasmonics. Ebbesen et al. first experimentally provided evidence of unusually high optical transmission with efficiency exceeding unity (a phenomenon known as extraordinary optical transmission (EOT)) through holey metal film in 1998<sup>[7]</sup> and demonstrate the possibility of overcoming a fundamental constraint, i.e., extremely low transmittivity of subwavelength apertures. Plasmon mediated transmission of light through subwavelength channels has inspired a great interest for many engineering applications ever since. EOT refers to the greatly enhanced optical transmission in an otherwise opaque metal film patterned with periodic structure and can be dominated by the diffraction and/or spoof plasmons. Another well-known transmission phenomenon namely elec-

tromagnetically induced transparency (EIT), however, refers to the resonant process observed in three-level atomic configurations, in which two optical beams are coherently coupled to two energy level transitions.<sup>[8]</sup> Due to the destructive interference between the amplitudes associated with different excitation pathways, the transmission of an optical beam can be greatly enhanced in a narrow frequency band. A metamaterial analogue of the atomic system is the coherent coupling between two deliberately designed resonant pathways in a single unit cell, where one supports the excitation of the so-called “bright mode” while the other the “dark mode.”<sup>[9]</sup> In fact, such EIT-like effect can be termed as plasmon-induced transparency in optical regime.<sup>[10]</sup> However, the maximal transparency achievable by the artificial system with resemblance to the atomic system is determined by the ratio of the line widths of the two resonance processes which is inherently limited by the metallic loss of the metamolecules. In view of such limitation, a suitable alternative is to combine the advantages of both worlds in a hybrid system where the broadband oscillation of plasmonic molecule can strongly interact with the narrowband absorption line of the dielectric and opens up a narrow transmission window through a process called hybridization-induced

## 1. Introduction

In the last few decades, the field of plasmonics received extensive attention of the researchers because of plasmon's unprecedented ability to couple free space electromagnetic excitation into nanoscale volume and manipulate light–matter interaction. With the recent advancement of nanotechnology, plasmonics has become the emerging research topic in energy

D. Hasan, C. P. Ho, Dr. C. Lee  
Department of Electrical and Computer Engineering  
National University of Singapore  
4 Engineering Drive 3, Singapore 117576, Singapore  
E-mail: elelc@nus.edu.sg

D. Hasan, C. P. Ho, Dr. C. Lee  
Center for Sensors and MEMS  
National University of Singapore  
4 Engineering Drive 3, Singapore 117576, Singapore

D. Hasan, C. P. Ho, Dr. C. Lee  
NUS Suzhou Research Institute (NUSRI)  
Suzhou Industrial Park  
Suzhou 215123, P. R. China



DOI: 10.1002/adom.201600014

transparency. The dielectric system can be represented by a wide range of solids, fluids, and gaseous materials and can be even substituted by quantum structures,<sup>[11,12]</sup> mechanical oscillators,<sup>[13,14]</sup> and phonon excitations.<sup>[15,16]</sup> Recently, a new phenomenon known as absorption-induced transparency (AIT) has been unveiled in such a metal–dielectric hybrid system, which roughly refers to the enhancement of transmittance through a metallic structure when a dye with resonant absorption is present in the vicinity of the structure.<sup>[17,18]</sup> The process involves the reduction in the opacity of metal film governed by the highly dispersive optical response of the dye at the absorption band frequency. The enhancement of transmission is associated with the reduction of the imaginary part of the propagation constant when the dye is present and thus has a localized character. Interestingly, due to the nonplasmonic nature, AIT effect can be obtained in any range of spectrum spanning from visible to terahertz wavelength by the appropriate selection of the dye. In this work, we demonstrate the existence of absorption-induced transparency at mid-IR in a quasi 3D device with volumetric field enhancement for the first time. The device consists of two metasurfaces derived by the Babinet's principle and self-aligned to each other with the help of a patterned layer of PMMA. By carefully selecting the dimensions of the device, we fix the spectral location of the evanescent mode around 5.79  $\mu\text{m}$  where the optical response of PMMA is strongly dispersive. The proposed configuration is significantly unique to the previous works as it does not rely on the integration of the dielectric overlayer with the metal patterns and thus provides enhanced access to the surrounding for interaction inside the 3D nanochannels. Besides, AIT effect can be deployed for new types of photothermally or thermo-optically activated telecommunication and energy harvesting devices.<sup>[19,20]</sup> Therefore, we also demonstrate the nonplasmonic refractive index sensing capability of the effect and its thermal tuning entirely relying on the conformational change of the molecular mode for the first time to the best of our knowledge.

## 2. Design, Fabrication and Characterization

In **Figure 1b**, we show the polarization independent configuration of the layout under normal incidence where each of the triangles is one of the four constituent arms of the device. The configuration is also useful to enhance the volumetric interaction with the sensing material on a given foot print as discussed later in the text. A self-symmetric cavity is etched into each triangle by connecting the mid points of the sides. While doing so, we provide two nanometric parameters: the narrow conduction path of width  $f$  (offset) and the split gap  $s$  in the layout as shown in **Figure 2b**. The narrow path is essential for strong manipulation of the surface current at the acute junctions of the geometry<sup>[21]</sup> and the split gap facilitates magnetic resonance in the structure. Magnetic-resonance-induced transparency

is attractive for manifold reasons such as fundamental study of weak magnetic dipole emission, magnetic optical detector, and metamaterials with enhanced reconfiguration.<sup>[22–24]</sup> By such inclusion of plasmonic cavity, we obtain three coherent radiators (I, II, and III) from one host triangle as shown in **Figure 1b**. Then, we obtain the complementary surface as shown in **Figure 1c** by subtracting the noncomplementary one from the uniform metal surface according to the Babinet's principle.

A 3D finite-difference time domain (FDTD) solver has been deployed on a 16 core, 2.60 GHz Intel Xeon ES-2670 (128 GB memory) processor to simulate the reflection and transmission spectrum at near field under X-polarized light. The near field transmittance has been captured by a transmission monitor placed 15  $\mu\text{m}$  away from the metal patterns. The simulation region has been terminated by periodic boundary condition along the  $x$  and  $y$  directions and PML along the  $z$  direction. A spatial resolution of  $dx = 1 \text{ nm}$ ,  $dy = 1 \text{ nm}$ , and  $dz = 1 \text{ nm}$  is chosen for accurate calculation. Optical properties of gold have been extracted from Palik and the refractive indices of Si and  $\text{SiO}_2$  have been fixed at 3.5 and 1.45, respectively.

In **Figure 2**, we mark the resonances supported by the complementary and the noncomplementary surfaces in the 3D FDTD simulated transmission spectra. As suggested by the Babinet's principle, the observed transmission peaks of the complementary surface correspond to the transmission dips of the noncomplementary surface. However, among the three distinct resonances within the wavelength range of interest, resonance I originates due to the complex interplay of the multiple resonance paths.<sup>[25,26]</sup> The sharp line width of this resonance can be explored further in the future study. On the contrary, resonance II is purely dipolar and resonance III is purely magnetic in the noncomplementary surface. The corresponding transmission peak of the complementary surface is associated with sharp field enhancement at the two horizontal (along  $x$ ) corners of the small triangle surrounded by the apertures of the two vertical (along  $y$ ) host triangles. The magnetism at resonance III appears due to the presence of the split gap in the noncomplementary layout and is associated with the electric field enhancement at the split gap as shown in **Figure 2a**. The

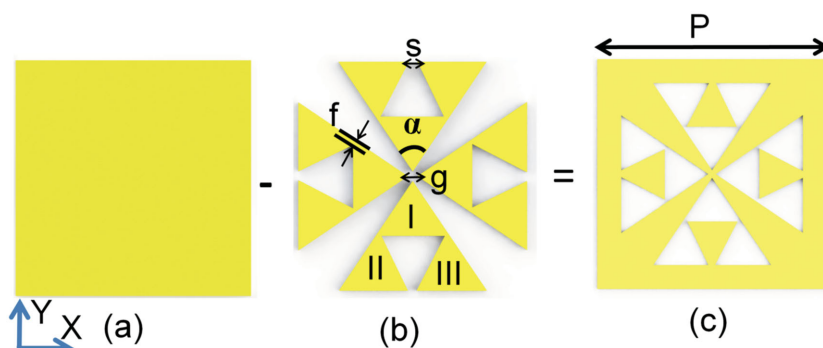


**Figure 1.** a) Uniform metal (Au) film, b) noncomplementary layout, c) complementary layout obtained by Babinet's principle. The coupling gap ( $g$ ) and the vertex angle ( $\alpha$ ) are fixed at 100 nm and  $30^\circ$ , respectively, unless otherwise stated. The period ( $p$ ) of the array is equal to 3  $\mu\text{m}$  unless otherwise stated. The height of each triangle has been kept constant at 2.55  $\mu\text{m}$  throughout the paper.

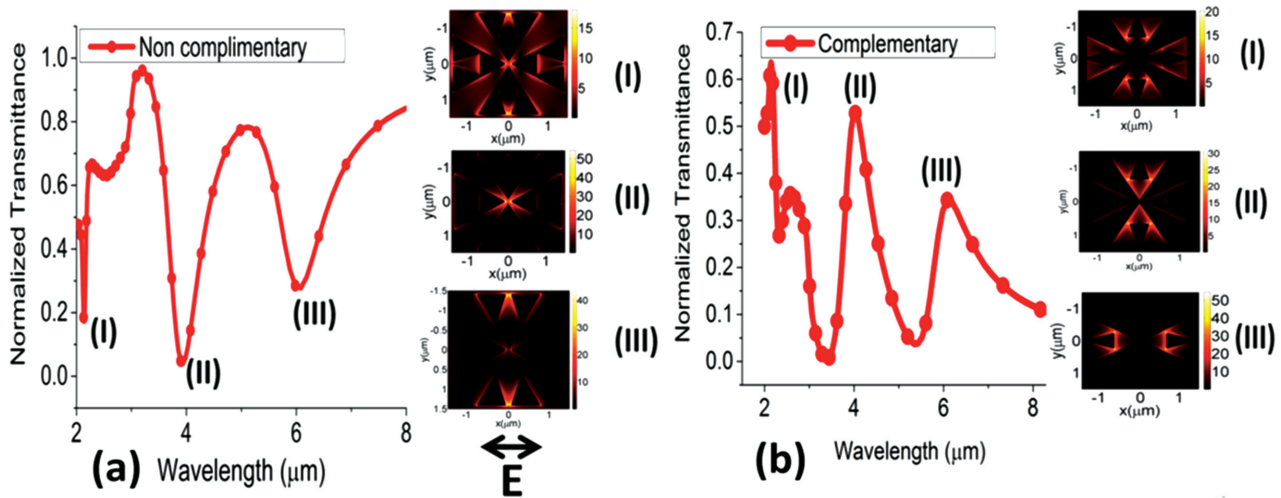


**Figure 2.** Normalized transmittance of a) noncomplementary and b) complementary surface along with the resonant *E*-field distribution. The parameters *f* and *s* are fixed at 70 and 100 nm, respectively, unless otherwise stated.

corresponding field distribution of the complementary layout is also shown in Figure 2b. The consistent contrast of the *E*-field distributions in Figure 2a,b between the noncomplementary and complementary cases is in strong agreement with the Babinet's principle. Note that there are two important resonant features of the noncomplementary and complementary surfaces on the blue side and the red side of the concerning PMMA transition at 5.79 μm. Alternatively, it can be argued that there exists an evanescent mode at 5.79 μm in the designed metasurfaces for the range of parameters being considered.<sup>[27]</sup> Figure 3a shows the conceptual 3D schematic of the vertically integrated metasurfaces self-aligned to each other. Figure 3b shows the

linking of the two patterns through the PMMA spacer. The cross section of the device is shown in Figure 3c.

The simplified process flow of the fabrication is shown in Figure 4. PMMA e-beam resist of thickness  $R_t$  is spin coated on a cleaned oxide substrate. We consider three different values of  $R_t$  (110, 180, and 250 nm) to study the coupling between the top and bottom layer. However, increasing  $R_t$  can strongly affect the fidelity of the sharp corners of the fractals due to the increased forward scattering range parameter of e-beam. The nanopatterns are written by a high resolution 100 KV ELS-7000 electron beam lithography equipment using raster scanning. The e-beam current is maintained at 200 pA.

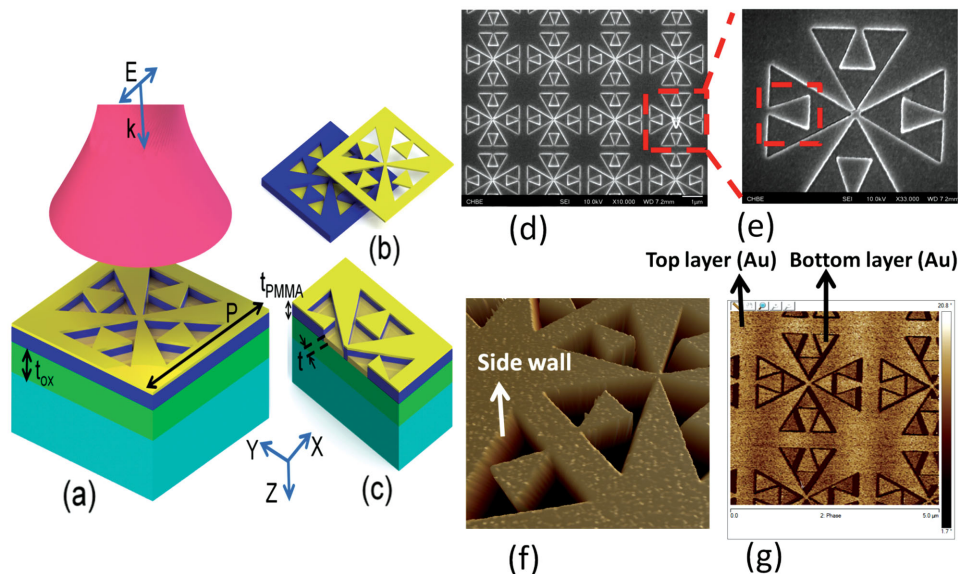


**Figure 3.** a) 3D schematic of the device, b) merging top and bottom layouts to obtain the quasi 3D configuration, c) cross section of the device, d) SEM image of the array of the device, e) zoomed in view of the quasi 3D device, f) AFM height profile of the structure in the quasi 3D configuration and g) AFM phase profile of the structure illustrating the dual Au layers. The substrate is Si coated with 1 μm thick ( $t_{ox}$ ) thermal oxide. PMMA thickness  $t_{PMMA}$  and gold thickness  $t$  is fixed at 180 and 35 nm, respectively, unless otherwise stated.

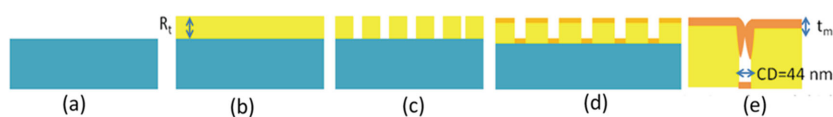


**Figure 4.** a–d) Simplified process flow. e) Issue of critical dimension and side walls due to the shadowing of metal evaporation.  $R_t$  is the e-beam resist thickness.

No proximity correction or indium tin oxide (ITO) charge compensation layer has been considered for the current batch of chips. Thus, the issue of back-scattering-induced corner roundedness may be crucial in some cases. The development time is controlled at 70 s in 1:3 MIBK:IPA solution. Finally, 5 nm of Cr layer followed by 35 nm of gold layer has been deposited by the Denton Explorer e-beam evaporator. Figure 3d shows the scanning electron microscopy (SEM) images of the large area nanopatterns obtained by a field emission SEM. The zoomed in view of the unit cells is shown in Figure 3e. Because of the 3D topography, we observe strong secondary electron emission from the edges of the geometries. Despite the high conformity of the e-beam deposition of metals, we suspect the presence of metal side walls due to the shadowing effect as shown in Figure 4e. To minimize the issue, a careful optimization between the metal thickness ( $t_m$ ) and the critical dimension is needed. We obtain the minimum feature size of 44 nm as shown in Figure 3e. The presence of such side wall can strongly affect the broadband resonances and introduce constant damping within the cavity partially formed by the two self-aligned reflecting layers. Finally, the 3D metal side walls have been investigated by a Bruker AFM with a Si tip of 5 nm radius. The results have been post processed by NanoScope Analysis and illustrated in Figure 3f. The AFM phase profile in Figure 3g shows the dual Au layers of the 3D device.

The normalized transmission and reflection spectra have been obtained by a broadband Agilent Fourier transform infrared (FTIR) spectroscopy. The area of the aperture is considered to be  $100 \mu\text{m} \times 100 \mu\text{m}$ . The reflectance of the devices is normalized with respect to that of a smooth gold surface and transmittance is normalized with respect to the free space

transmission of light. The size of the aperture was adjusted carefully to match with the size of each square pattern, therefore eliminating the background reflection. The sampling resolution is maintained at  $4 \text{ cm}^{-1}$  to minimize the presence of water absorption peaks although  $\text{CO}_2$  peak at  $4.26 \mu\text{m}$  can appear in the spectrum depending on the ambient concentration. The mirror repetition rate is fixed at 40 kHz and the number of scans is maintained to be 64.

## 3. Results and Analysis

### 3.1. Absorption-Induced Transparency

The vibrational transition of PMMA is modeled using the following Lorentzian equation<sup>[28]</sup>

$$n = \sqrt{\epsilon_o + \frac{\epsilon_{\text{lorenz}} \omega_o^2}{\omega_o^2 - 2i\gamma\omega - \omega^2}} \quad (1)$$

where  $\epsilon_o$  and  $\epsilon_{\text{lorenz}}$  is set at 1.00 and 0.04, respectively and  $\omega_o$  corresponds to the vibrational mode wavelength which is  $5.79 \mu\text{m}$ . The line width of the mode ( $\gamma$ ) is set at  $8 \times 10^{11} \text{ rad s}^{-1}$ .

**Figure 5** shows the existence of AIT peak in experiment and simulation. It can be observed in Figure 5c,d that the spectral position and the strength of AIT peak in experiment and simulation under normal incidence are qualitatively in agreement to each other. Two more additional EOT-like peaks adjacent to the AIT observed in Figure 5a,b are originated from the top metasurface as discussed previously and shown later in the text. Between the peaks, the structure permits nonresonant transmission of light through the apertures while the evanescent modes are bound at the surface. Hence, the resonant scattering mediated transmission expression  $t = (1 - \rho^2)e^{ik_z t_m} / (1 - \rho^2 e^{2ik_z t_m})$  can be approximated as  $t = (1 - \rho^2)e^{ik_z t_m}$  excluding the round trip build up of energy, where  $k_z$  is the propagation constant,  $t_m$  is the metamaterial thickness, and  $\rho$  is the reflection from the first interface.<sup>[29,30]</sup> It has been analytically shown in ref. [17] that the transmission enhancement on the onset of AIT occurs due to the reduction of the imaginary component of  $k_z$ . Such reduction eventually reduces the decay of the evanescent mode as it travels through the waveguide apertures and so, a peak is observed in the transmission spectrum. A similar description of the transmission by the hybrid triangular apertures discussed by this work will be analytically challenging. Nevertheless, it can be convincingly argued with the help of the following results that the AIT peak is solely generated due the presence of PMMA vibrational peak. The significance of the AIT peak obtained from the structure can be established further by running experiment on a 110 nm bare film of PMMA coated on oxide substrate. A transmission dip is observed at the transition wavelength as expected although a redshift

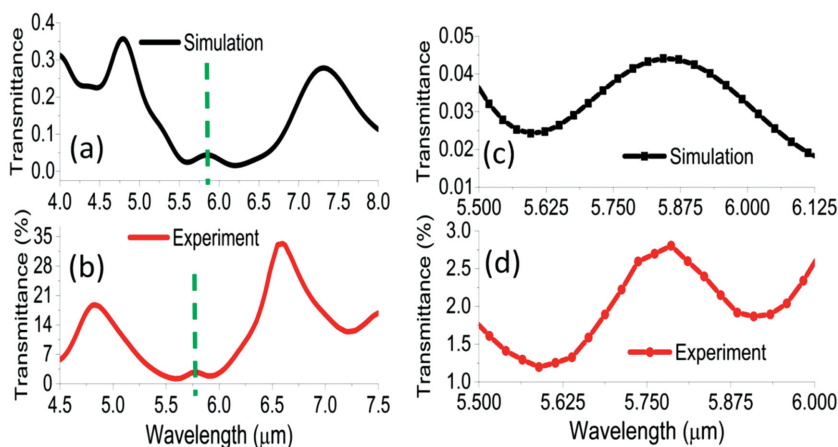


**Figure 5.** Resonant transmission peaks around the AIT peak (dashed green line) a) simulation and b) experiment. Zoomed in AIT peak c) simulation and d) experiment.

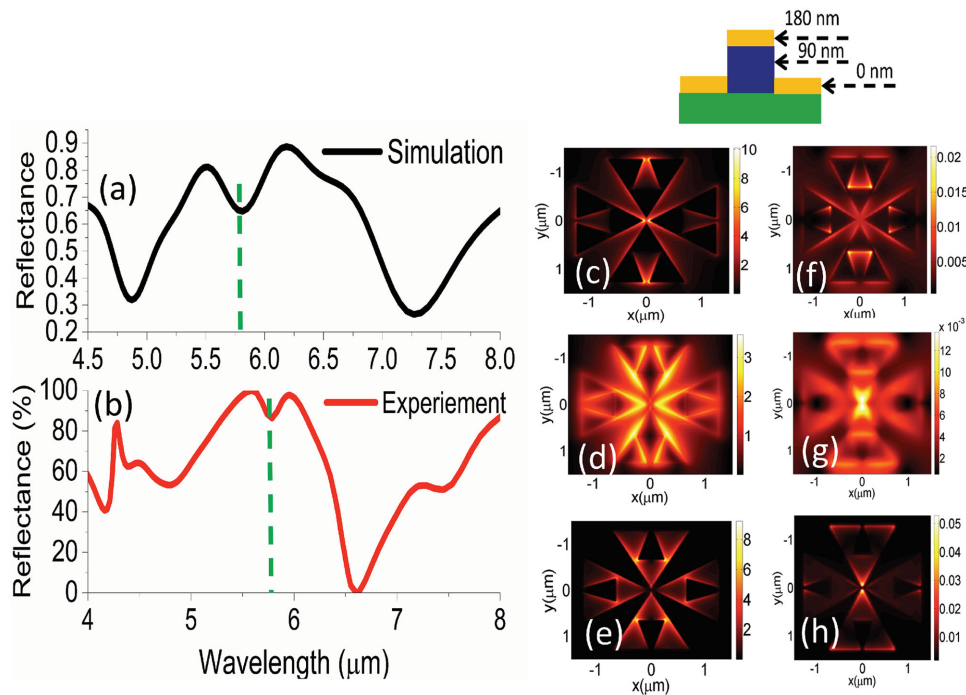


**Figure 6.** Resonant reflection dip at the AIT wavelength (dashed green line) a) simulation and b) experiment. *E*-field distribution at c) 0 nm, d) 90 nm, and e) 180 nm plane. *H*-field distribution at f) 0 nm, g) 90 nm, and h) 180 nm plane.

of 3 nm is observed in the AIT peak (Figure S1, Supporting Information).

Figure 6a,b shows the reflectance dip in simulation and experiment, respectively, at the AIT wavelength. The reflection spectrum is captured under normally incident X-polarized light in simulation while under unpolarized 45° oblique incidence in the FTIR. Despite the evolution of a transmission peak, the absorption by the structure reaches a maximum at the AIT wavelength (Figure S2, Supporting Information). The transmission peak is found to be independent of the polarization angle under normal incidence (Figure S3, Supporting Information). The experimentally observed dependence of polarization angle under 45° incidence is obtained using a polarizer (Figure S4, Supporting Information).

The *E*-field and *H*-field distributions in Figure 6c–h show the dipolar and magnetic behavior of the structure at the AIT

wavelength. The fields go through a complex transformation of amplitude and phase in the stacked geometry making the whole configuration more sensitive to any optical perturbation.<sup>[31]</sup> In fact, the tailorable dipolar and magnetic response of the structure while preserving the AIT effect can be considered for a new platform of multiplexed sensing based on both resonant and nonresonant process.

### 3.2. Material Dependence

To emphasize on the hybrid nature of the device, a proof-of-concept simulation result is shown in Figure 7a where the vibrational transition of PMMA is omitted and an artificial spacer layer of refractive index 1.49 is assumed. Clearly, the AIT peak disappears in the spectrum now. Thus, it becomes obvious that the strong dispersion of PMMA is primarily responsible for the strong modulation of the propagation constant and generation of the AIT peak. To justify the requirement of the evanescent mode further, we artificially sweep the vibrational frequency (i.e., wavelength) of the Lorentzian equation. It can be observed in Figure 7b that as the vibrational wavelength approaches the nearby EOT-like peak, the expected peak at AIT is transformed into a dip. This is so because multiple scattering in the structure enhances the absorption coming from the PMMA dye when a resonant plasmonic mode exists around the vibrational

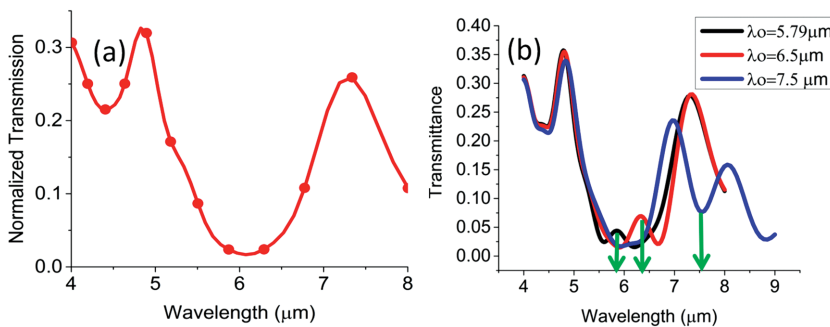


**Figure 7.** a) Disappearance of AIT peak as the vibrational absorption is excluded from the simulation model. b) Evolution of AIT peak into a dip as the vibration mode is redshifted.

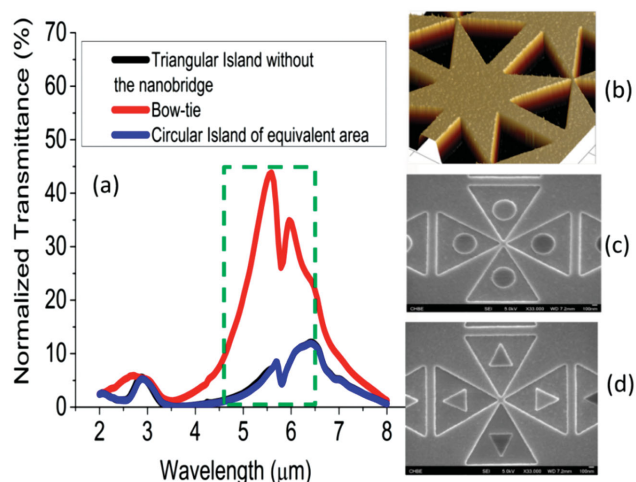


**Figure 8.** Structural dependence of the AIT peak. a) A transmission dip instead of the peak is observed around  $5.79 \mu\text{m}$  due to the spectrally overlapped plasmonic mode of the structures. b) The state-of-the-art bow-tie structure is considered without any inclusion. Two other variations are considered with c) circular and d) triangular inclusion. All the cases support EOT-like mode overlapped with the PMMA absorption.

wavelength. The amplitude of the AIT peak is apparently enhanced at  $6.5 \mu\text{m}$  with respect to the amplitude at  $5.79 \mu\text{m}$ . This occurs as the metal transmission is found to be larger at  $6.5 \mu\text{m}$  in Figure 7a.

### 3.3. Structural Dependence

Figure 8 shows the extended results on the requirement of evanescent mode as discussed in Figure 7b. Three unique cases are considered: (i) conventional bow-tie metasurface without any inclusion (Figure 8b), (ii) bow-tie metasurface with circular island (Figure 8c), and (iii) bow-tie metasurface with triangular island (Figure 8d). The areas of the islands in cases (ii) and (iii) are roughly equal to the area of the plasmonic inclusion of this work. It can be observed in Figure 8a that all three cases support a broadband plasmonic mode as indicated by the green dashed rectangle. However, due to the resonant effect of these modes, the intrinsic absorption of PMMA becomes activated and a transmission dip overlaps with the plasmonic mode in the spectrum. The Fano-like asymmetry of the dip is visible because of the strong coupling between the broadband plasmonic mode and the narrowband absorption line of PMMA.<sup>[32]</sup>

### 3.4. Study of Parameters

In the following discussions, we experimentally study the parametric dependence of AIT effect in the proposed geometry. Please note that the parameter  $f$  can strongly influence the dipolar and magnetic surface current distribution of the structure. By increasing  $f$ , we also reduce the area of the apertures of the device. Interestingly, a consistent increase of maximum transmission is observed in Figure 9a as  $f$  is increased. Such

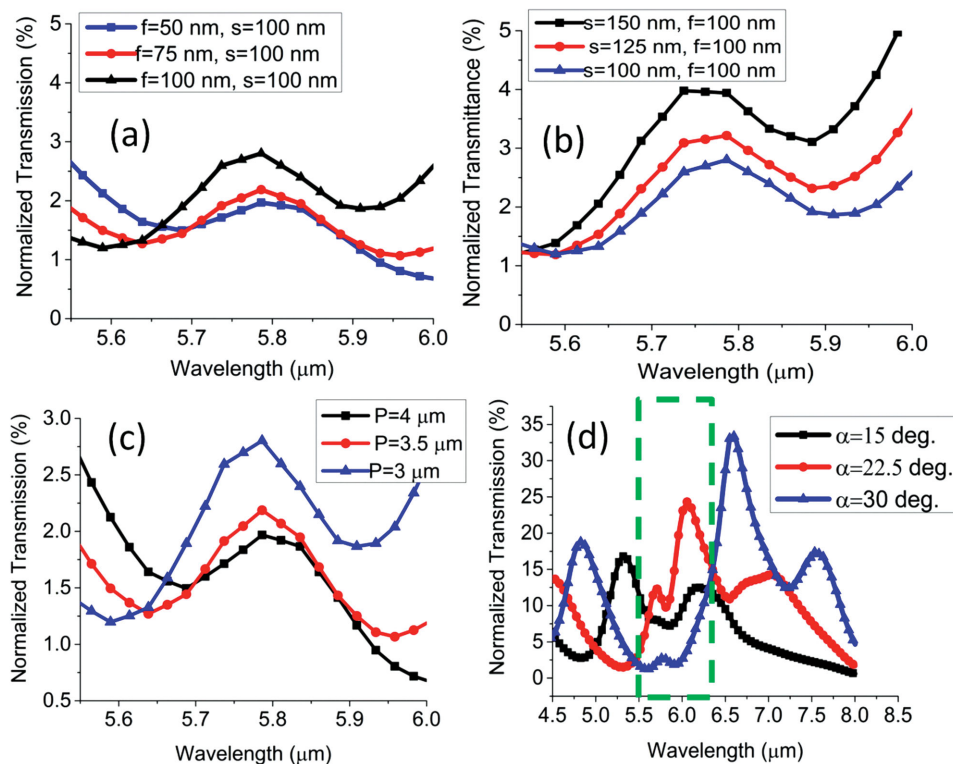


**Figure 9.** Structural dependence of AIT peak a) variation of offset  $f$ , b) variation of split gap  $s$  c) variation of periodicity  $P$ , and d) variation of vertex angle  $\alpha$ .

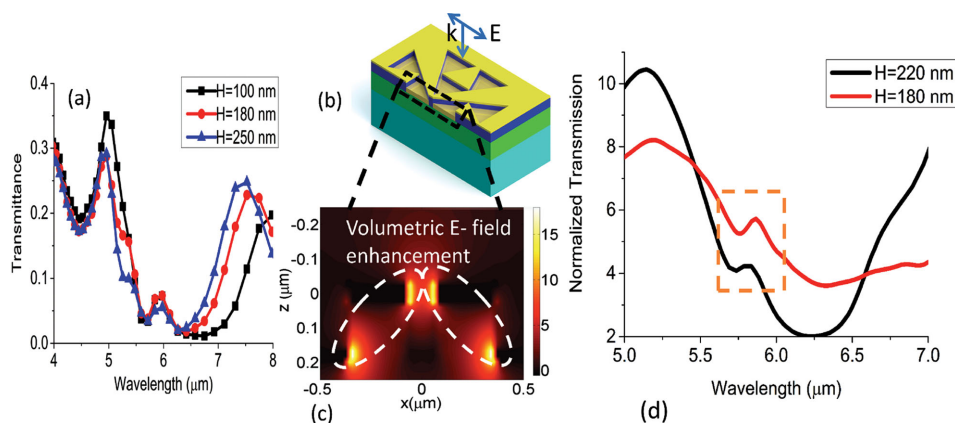


**Figure 10.** a) Simulated effect of coupling distance between the two layers. b) Cross section showing the coupled top and bottom layer. c) Volumetric field enhancement across the plane shown in (b). d) Experimentally observed effect of varying coupling distance on the AIT wavelength refractive index sensitivity of the AIT peak (c) electromagnetic energy coupling between the top and bottom layer at AIT wavelength.

increment can be ascribed to the decrease of  $\text{Im}(k_z)$  as the peak transmission can be expressed as  $T_{\text{max}} \propto \exp[-2\text{Im}(k_z)t_m]$  for the least order of evanescent mode. Similarly, for the increase of the split gap  $s$ , we observe a regular relationship with the peak transmission in Figure 9b. It is noteworthy that apparently no change of the spectral location of the AIT peak is observed due to the geometric modification which again implies the localized nature of the effect.

Next, we vary the periodicity of the structure. It is decisive from the results in Figure 9c that the strength of the AIT peak is a strong function of the array periodicity. The periodicity introduces a transverse resonance with wave vector  $k_c = \frac{2\pi}{P}$  and can enhance or inhibit the transmission of the structure.<sup>[33]</sup> Here, it can be observed that the absorption-induced transparency can be increased to some extent by reducing the periodicity, i.e., by making the arrangement of the unit cells more closely packed. Yet, no change of the spectral location of the AIT peak is observed as the periodicity is changed. Finally, we investigate the role of vertex angle on tuning the characteristics of the AIT peak. Vertex angle is a unique parameter of the bow-tie structure that provides a relatively more sensitive degree of freedom for tuning the resonant transmission. It can be observed in Figure 9d that a regular blueshift of the plasmonic modes on the red side of the AIT position occurs as the vertex angle is scaled down. As explained previously, transmission dip instead of the peak appears at the AIT position as soon as a plasmonic mode is spectrally overlapped with the AIT wavelength.

One of the unique features of the design is the vertical coupling between the top and bottom metal layer along with the volumetric field enhancement as shown in **Figure 10b,c**. The coupling distance between the top and bottom layers is defined by the PMMA thickness. The simulated results in Figure 10a show no spectral change of the AIT peak as the distance is increased although the adjacent resonant peaks are strongly blueshifted. Such resonance shift can be partially addressed by the theory of optical circuits.<sup>[34,35]</sup> As the spacing is decreased, the capacitance ( $C$ ) induced between the two layers can be increased, thereby redshifting the resonance location of the

modes as determined by  $\lambda \propto \sqrt{LC}$ , where  $L$  is the inductance. Finally, the experimental confirmation of the nonresonant characteristics of the AIT effect as the coupling distance is varied is provided in Figure 10d. This result implies that AIT is a localized phenomenon and primarily an outcome of the modification of the propagation constant of the evanescent mode.

### 3.5. Nonplasmonic and Volumetric Refractive Index Sensing

**Figure 11a** shows the four quasi 3D nanochannels of the device that support the AIT peak.

Despite being a nonplasmonic effect, a strong dependence of the AIT peak on the background index is observed in Figure 11b. In fact, a RIU shift of 600 nm is observed in simulation indicating strong sensitivity of the effect in the quasi 3D configuration.<sup>[36]</sup> The full width at half maximum (FWHM) of the peak is 287 nm yielding a figure of merit (FOM) of 2.09. The origin of the shift of the nonresonant process is related to the effective dielectric constant of an infiltrated metal pattern expressed as below<sup>[17]</sup>

$$\tilde{\epsilon} = [\epsilon_A - (\lambda/\lambda_c)^2]/S^2 \quad (2)$$

where  $\epsilon_A$  is the permittivity of the filling material,  $\lambda_c$  is the cutoff wavelength of the waveguide, and  $S$  is the effective magnetic susceptibility that depends on the structure and metal properties. We argue that the parameters in Equation (2) can be modulated by a change of dielectric constant causing a shift in the spectrum according to the effective medium theory.<sup>[37]</sup> In this case, increasing the background index can redshift the peak transmission wavelength. In fact, the sets of quasi 3D nanochannels in one unit cell can be efficiently deployed for volumetric refractive index sensing in microfluidic applications.<sup>[38,39]</sup> In Figure 11d, we demonstrate using the quasi 3D device a multiplexed mid-IR spectroscopy of a sensing material modeled as in Figure 11c. The role of the nanochannels on the overall sensitivity of the device becomes obvious as they are

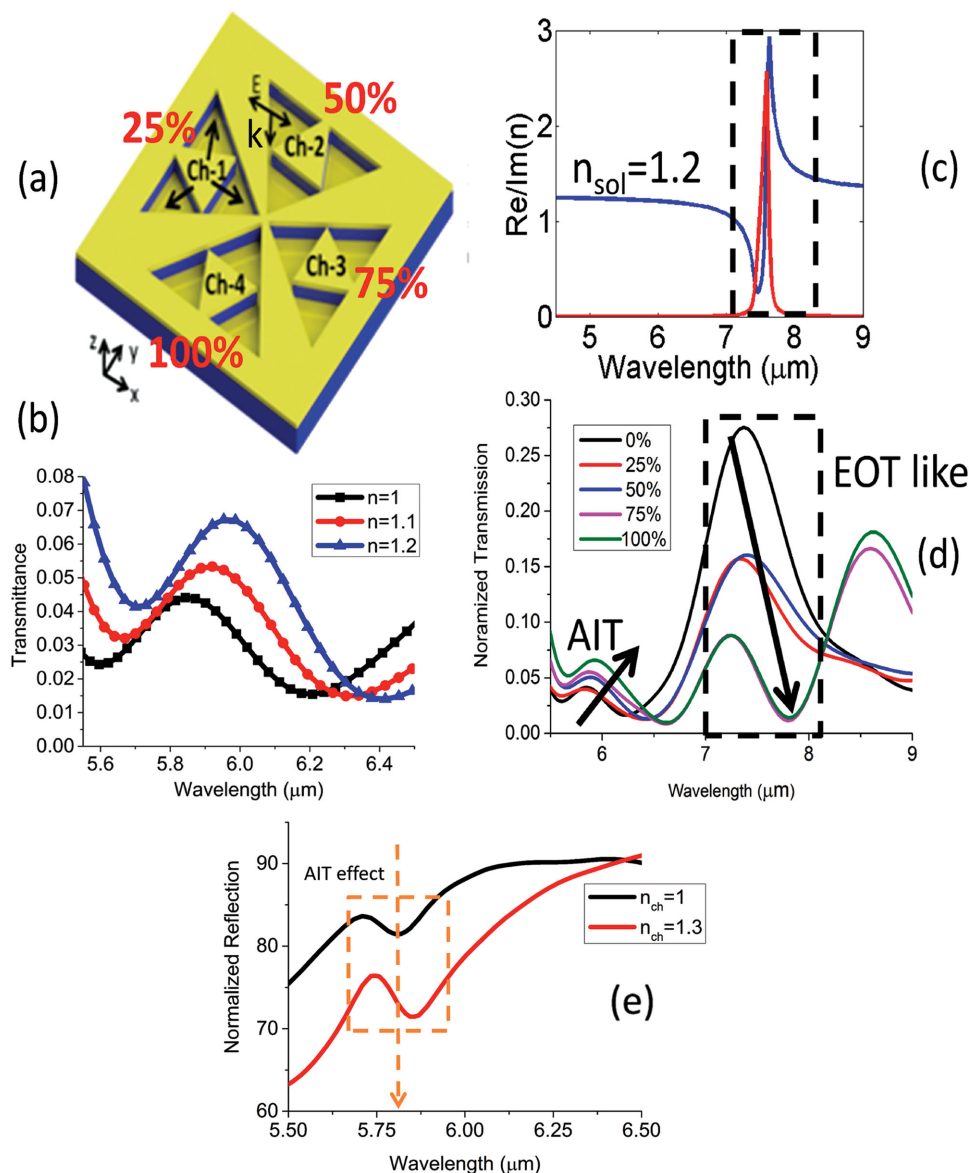


**Figure 11.** a) Illustration of the four nanochannels in the device. b) Simulated shift of the AIT peak as the background refractive index is increased. c) Refractive index profile of the sensing material possessing an absorption peak at  $7.3 \mu\text{m}$ . d) Role of the nanochannels on achieving multiplexed sensing. The AIT peak is responsive to the solution refractive index whereas the EOT-like peak captures the absorption signal. e) Experimental confirmation of the shift of the AIT peak when the sample is rinsed in DI water.

sequentially infiltrated (25%, 50%, 75%, and 100%). The total RIU shift in this case is  $395 \text{ nm}$  yielding an FOM of 1.376. Here, the AIT peak is particularly responsive to the refractive index of the solution providing valuable information on the amount of the infiltrated samples. Note that the volume of each channel is  $0.1545 \mu\text{m}^3$ , meaning a total volume of  $800 \mu\text{m}^3$  in a foot print of  $100 \times 100 \mu\text{m}^2$  consists of the highly dense nanopatterns for refractive index sensing. Such volumetric interaction is not available in the conventional 2D plasmonic devices. Figure 11e shows the experimentally observed redshift of the AIT effect after rinsing the sample in deionized (DI) water. The RIU redshift experimentally obtained is  $123.33 \text{ nm}$ . The experimental result is in agreement with the effective medium consideration (redshift) as discussed previously and indicates the

possibility of the nonresonant AIT effect for sensing application for the first time.

### 3.6. Thermally Tunable Absorption-Induced Transparency

To this end, we demonstrate thermal tuning of the absorption-induced transparency for the first time to the best of our knowledge. The sample is placed on a heating stage, which is capable of heating up to  $450 \text{ }^\circ\text{C}$ . The temperature within the stage is controlled by a temperature controller with a variation of less than 5%. The sample chamber is properly insulated from the ambience. The measurement is taken 5 min after the stable reading of a particular temperature is

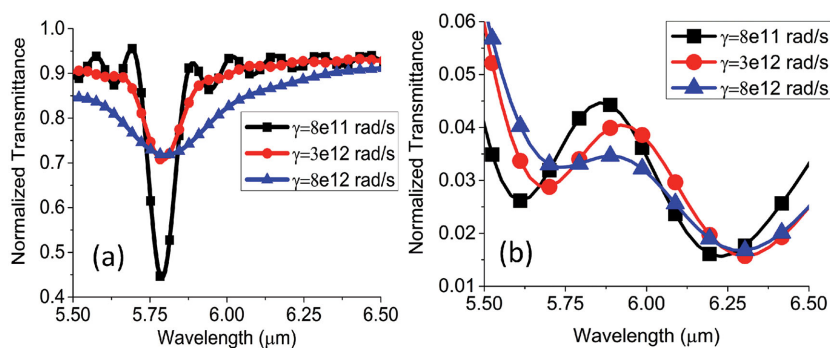


**Figure 12.** a) Effect of line width broadening on transmission dip of PMMA thin film. b) Effect of broadening on the strength and spectral position of the AIT peak.

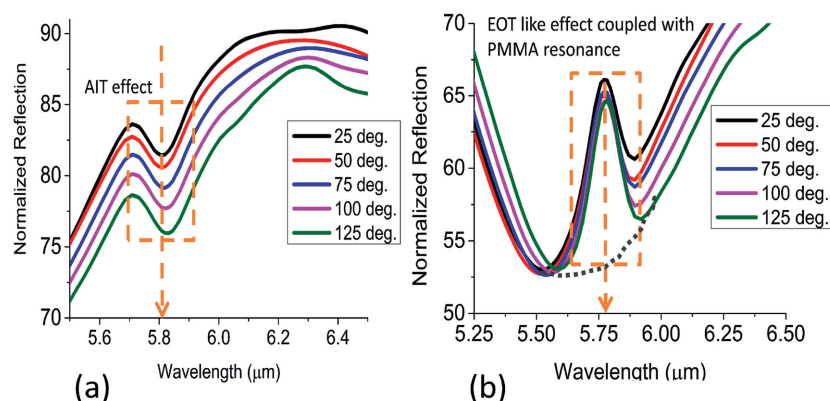


**Figure 13.** Temperature-dependent comparison between a) AIT effect and b) EOT-like effect when it is coupled with PMMA resonance in reflection mode. The grey dot line predicts the profile of the EOT resonance if the PMMA absorption is absent. Here, the geometry in Figure 8b is considered as a representative for the EOT-like effect.

reached. In the current setup, only reflection signal can be captured while the heating stage is incorporated. Temperature-induced homogeneous broadening of the vibrational line width of PMMA offers a mechanism for thermal tuning of the composite device. Under homogeneous premise, the temperature dependence of vibrational line width  $\gamma(T)$  follows a power law  $\gamma(T) \propto T^\alpha$ , where the exponent  $\alpha$  is greater than 1.<sup>[40,41]</sup> Here, we increase  $\gamma$  in the Lorentzian model from its room temperature value of  $8 \times 10^{11} \text{ rad s}^{-1}$  and observe the corresponding impact. **Figure 12a** shows the broadening of the transmission dip in PMMA thin film along with a pronounced intensity decrease as the line width is increased. However, no resonance shift is observed which is in agreement with the experimental result (Figure S5, Supporting Information). Interestingly, such broadening can introduce a shift of the AIT peak as shown in Figure 12b. Such shift is associated with the change in intensity of the Lorentzian distribution of  $\text{Re}(n)$  and  $\text{Im}(n)$ . **Figure 13a** provides the experimental confirmation of the thermal tuning of the AIT effect in the reflection mode. We achieve a tuning of 25 nm for a moderate range of temperature increase (100°) which is also reversible. The regular base line shift observed is due to the change of DC conductivity of metal in the nonresonant

regime.<sup>[42]</sup> Figure 13b shows the case when a resonant EOT-like mode is coupled with the PMMA absorption and gives rise to the asymmetric profile.<sup>[43]</sup> In contrast to the AIT effect, no resonance shift is observed as the temperature is increased. Besides, a complex change of quality factor of the coupled mode and intensity variation is observed on the blue and red side of the peak. This is due to the interplay of the temperature-dependent behavior of the resonant EOT mode and PMMA absorption. Thus, we demonstrate, for the first time, thermal tuning of a nonresonant effect which is entirely based on the conformational change of the molecular mode.

## 4. Discussion

In summary, we demonstrate thermally tunable absorption-induced transparency at mid-IR on a quasi 3D bow-tie nanostructure for volumetric and nonplasmonic refractive index sensing for the first time. The design is derived from the Babinet's principle and provides multiple parameters to tailor the dipolar and magnetic response for a new generation of multiplexed sensing protocol based on resonant and nonresonant process. Realization of the proposed device only requires a single-step lithography followed by a single metal deposition and no liftoff and does not depend on the accuracy of multilayer alignment. Thus, the idea is technologically more viable for mass deployment of large area mid-IR sensors in a multianalyte environment. Here, we confirm the nonplasmonic and localized nature of the AIT peak with the help of the extensive amount of experimental and theoretical results. We adopt a semianalytical approach to assure the mutual contribution of the evanescent mode and vibrational mode toward the origin of AIT phenomenon and to establish the nonresonant nature of the process. In addition, we thoroughly discuss several physical parameters relevant to the proposed nanoarchitecture such as array periodicity, aperture size, and vertical coupling. Refractive index sensitivity analysis shows that the AIT effect on the quasi 3D platform can be a new alternative for solution based detection despite the nonresonant characteristics. We experimentally obtain a RIU shift of 123.33 nm by the process for the first time in literature. We also demonstrate a thermal tuning of 25 nm within the temperature range limited by the glass transition point of PMMA. We believe that the proposed hybrid structure will lay a foundation for AIT based photo-thermally/thermo-optically triggered photonic devices in the arenas of telecommunication and energy harvesting applications harnessing the transient/permanent change of molecular configuration in the near future.

## Supporting Information

Supporting Information is available from the Wiley Online Library or from the author.

## Acknowledgements

The authors acknowledge the financial support from the research grant of MOE/NUS, ARF-Tier 2 (MOE2012-T2-2-154; NUS WBS: R-263-000-A59-112) "Monolithic integrated Si/AlN nanophotonics platform for optical NEMS and OEICs" at the National University of Singapore, and the partial support by National Natural Science Foundation of China under Grant No. 61474078 at NUS (Suzhou) Research Institute, Suzhou, China.

Received: January 10, 2016

Published online: March 9, 2016

- [1] N. Karker, G. Dharmalingam, M. A. Carpenter, *ACS Nano* **2014**, *8*, 10953.
- [2] D. Dregely, K. Lindfors, M. Lippitz, N. Engheta, M. Totzeck, H. Giessen, *Nat. Commun.* **2014**, *5*, 4354.
- [3] X. Xu, D. Hasan, L. Wang, S. Chakravarty, R. T. Chen, D. L. Fan, A. X. Wang, *Appl. Phys. Lett.* **2012**, *100*, 191114.
- [4] X. Xu, H. Li, D. Hasan, R. S. Ruoff, A. X. Wang, D. L. Fan, *Adv. Funct. Mater.* **2013**, *23*, 4332.
- [5] F. Ren, J. Campbell, D. Hasan, X. Wang, G. L. Rorrer, A. X. Wang, in *Proc. CLEO: Science and Innovations*, OSA Publishing, Washington, DC, USA **2013**, p. 1.
- [6] D. Hasan, C. P. Ho, P. Pitchappa, C. Lee, *ACS Photonics* **2015**, *2*, 890.
- [7] T. W. Ebbesen, H. J. Lezec, H. F. Ghaemi, T. Thio, P. A. Wolff, *Nature* **1998**, *391*, 667.
- [8] M. Fleischhauer, A. Imamoglu, J. P. Marangos, *Rev. Mod. Phys.* **2005**, *77*, 633.
- [9] R. Taubert, M. Hentsche, J. Käste, H. Giessen, *Nano Lett.* **2012**, *12*, 1367.
- [10] P. Weis, J. L. Garcia-Pomar, R. Beigang, M. Rahm, *Opt. Express* **2011**, *19*, 23573.
- [11] C. Walther, G. Scalari, M. I. Amanti, M. Beck, J. Faist, *Science* **2010**, *327*, 1495.
- [12] X. Wu, S. K. Gray, M. Pelton, *Opt. Express* **2010**, *18*, 23633.
- [13] P. Li, S. Gao, F. Li, *Phys. Rev. A* **2013**, *88*, 043802.
- [14] J. D. Teufel, D. Li, M. S. Allman, K. Cicak, A. J. Sirois, J. D. Whittaker, R. W. Simmonds, *Nature* **2011**, *471*, 204.
- [15] F. Neubrech, D. Weber, D. Enders, T. Nagao, A. Pucci, *J. Phys. Chem. C* **2010**, *114*, 7299.
- [16] D. J. Shelton, I. Brener, J. C. Ginn, M. B. Sinclair, D. W. Peters, K. R. Coffey, G. D. Boreman, *Nano Lett.* **2011**, *11*, 2104.
- [17] S. G. Rodrigo, F. J. Garcia-Vidal, L. Martín-Moreno, *Phys. Rev. B* **2013**, *88*, 155126.
- [18] J. A. Hutchison, D. M. O'Carroll, T. Schwartz, C. Genet, T. W. Ebbesen, *Angew. Chem. Int. Ed.* **2011**, *50*, 2085.
- [19] J. Gosciniaik, S. I. Bozhevolnyi, T. B. Andersen, V. S. Volkov, J. Kjølstrup-Hansen, L. Markey, A. Dereux, *Opt. Express* **2010**, *18*, 1207.
- [20] C. Weeber, K. Hassan, L. Saviot, A. Dereux, C. Boissière, O. Durupthy, C. Chaneac, E. Burov, A. Pastouret, *Opt. Express* **2012**, *20*, 27636.
- [21] E. Prodan, C. Radloff, N. J. Halas, P. A. Nordlander, *Science* **2003**, *302*, 419.
- [22] S. M. Hein, H. Giessen, *Phys. Rev. Lett.* **2013**, *111*, 026803.
- [23] L. Aigouy, A. Cazé, P. Gredin, M. Mortier, R. Carminati, *Phys. Rev. Lett.* **2014**, *113*, 076101.
- [24] S. Linden, C. Enkrich, M. Wegener, J. Zhou, T. Koschny, C. M. Soukoulis, *Science* **2004**, *306*, 1351.
- [25] B. Lee, J. Park, G. H. Han, H. Ee, C. H. Naylor, W. Liu, A. T. C. Johnson, R. Agarwal, *Nano Lett.* **2015**, *15*, 3646.
- [26] D. Wei, B. Renaud, K. Sergei, R. Pascal, E. de Lamaestre Roch, *J. App. Phys.* **2010**, *108*, 124314.
- [27] R. Gordon, A. G. Brolo, D. Sinton, K. L. Kavanagh, *Laser Photonics Rev.* **2010**, *4*, 311.
- [28] B. Lahiri, S. G. McMeekin, R. M. De La Rue, N. P. Johnson, *Opt. Express* **2013**, *21*, 9343.
- [29] L. Martín-Moreno, F. J. García-Vidal, H. J. Lezec, K. M. Pellerin, T. Thio, J. B. Pendry, T. W. Ebbesen, *Phys. Rev. Lett.* **2001**, *86*, 1114.
- [30] F. J. Garcia-Vidal, L. Martín-Moreno, T. W. Ebbesen, L. Kuipers, *Rev. Mod. Phys.* **2010**, *82*, 729.
- [31] M. E. Stewart, N. H. Mack, V. Malyarchuk, J. A. N. T. Soares, T. Lee, S. K. Gray, R. G. Nuzzo, J. A. Rogers, *Proc. Natl. Acad. Sci. USA* **2006**, *103*, 17143.
- [32] B. Luk'yanchuk, N. I. Zheludev, S. A. Maier, N. J. Halas, P. Nordlander, H. Giessen, C. Tow Chong, *Nat. Mater.* **2010**, *9*, 707.
- [33] B. Lee, J. Park, G. H. Han, H. Ee, C. H. Naylor, W. Liu, A. T. C. Johnson, R. Agarwal, *Nano Lett.* **2015**, *15*, 3646.
- [34] Y. Sun, B. Edwards, A. Alù, N. Engheta, *Nat. Mater.* **2012**, *11*, 208.
- [35] P. C. Wu, W. Hsu, W. T. Chen, Y. Huang, C. Liao, A. Liu, N. I. Zheludev, G. Sun, D. Tsai, *Sci. Rep.* **2015**, *5*, 9726.
- [36] Y. Shen, J. Zhou, T. Liu, Y. Tao, R. Jiang, M. Liu, G. Xiao, J. Zhu, Z. Zhou, X. Wang, C. Jin, J. Wang, *Nat. Commun.* **2013**, *4*, 2381.
- [37] G. A. Niklasson, C. G. Granqvist, O. Hunderi, *Appl. Opt.* **1981**, *20*, 26.
- [38] F. De Angelis, M. Malerba, M. Patrini, E. Miele, G. Das, A. Toma, R. P. Zaccaria, E. D. Fabrizio, *Nano Lett.* **2013**, *13*, 3553.
- [39] J. Wang, W. Zhou, J. Zhang, M. Yang, C. Ji, X. Shao, L. Shi, *Microelectron. Eng.* **2014**, *115*, 2.
- [40] K. A. Tokmakoffa, M. D. Fayer, *J. Chem. Phys.* **1995**, *103*, 2810.
- [41] J. Kaminský, P. Bour, J. Kubelka, *J. Phys. Chem. A* **2011**, *115*, 30.
- [42] M. Bosman, L. Zhang, H. Duan, S. Tan, C. A. Nijhuis, C. Qiu, J. K. W. Yang, *Sci. Rep.* **2014**, *4*, 5537.
- [43] F. Cheng, X. Yang, J. Gao, *Sci. Rep.* **2015**, *5*, 14327.